Journal Name

RSCPublishing

COMMUNICATION

Cite this: DOI: 10.1039/x0xx00000x

Raman spectroscopic study of the carbon deposition mechanism on Ni/CGO electrodes under CO/CO_2 electrolysis

V. Duboviks,[a±] R. C. Maher,[b] M. Kishimoto,[a] L. F. Cohen[b] and N. P. Brandon[a], G. J. Offer[c]

Received 00th January 2012,
Accepted 00th January 2012

DOI: 10.1039/x0xx00000x

www.rsc.org/

***In situ* and *ex situ* Raman analysis of porous Ni/CGO electrodes reveal differences in amount, location and type of carbon formed during CO/CO_2 electrolysis. The results demonstrate the limitations of optical *in situ* techniques applied to Solid Oxide Cells (SOCs) operated in electrolysis conditions. Increased carbon deposition close to the electrode-electrolyte interface is likely to be the result of high charge-transfer current in that area. The positive effect of a CGO interlayer on reducing carbon formation on the fuel electrode is demonstrated.**

Solid oxide electrolysis cells (SOECs) are promising devices for simultaneous electrolysis of steam and carbon dioxide for synthetic gas production.[1–6] However, a long-term deactivation of the fuel electrode during co-electrolysis has been reported.[7] One of the most prominent degradation mechanisms in SOCs (Solid Oxide Cells) is a change in microstructure and active site deactivation due to carbon deposition.[8–14] Thermodynamically, carbon formation is preferentially favoured at low temperatures (500-700 °C).[15,16] However, carbon formation at the electrode-electrolyte interface in co-electrolysis conditions has been demonstrated for nickel/yttria stabilised zirconia (Ni/YSZ) electrodes operating at high current density even at 875 °C.[13] Despite the fact that carbon formation is not predicted thermodynamically at fuel conversion below 99% for these conditions, it was experimentally observed at a conversion rate of only 67%.[13] This indicates the importance of accounting for kinetic effects when studying carbon formation in SOCs.

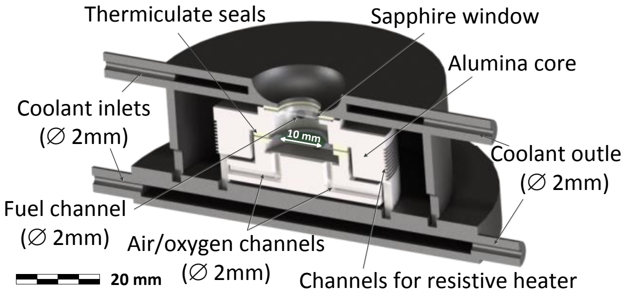

Fig. 1 Cross-sectional 3D parametric view of the micro-SOFC rig with optical access for Raman measurements.

For SOC technology to be commercially viable a decrease in the operating temperature from 900 °C to 500-600 °C would reduce material costs and enable easier coupling with external heat sources.[17,18] In general, the Ni/$Ce_{0.9}Gd_{0.1}O_{1.95}$ (Ni/CGO) system has been identified as one of the most promising fuel electrode material systems both in terms of its catalytic properties and reduced carbon formation, when operating with carbonaceous species both in electrolysis[19] and fuel cell conditions.[20] The ability of CGO to release oxygen is used to explain the superior carbon tolerance of CGO-based electrodes in fuel cell conditions.[21] Equally, the durability of Ni-YSZ electrode impregnated with CGO has been shown to increase when compared to bare Ni-YSZ in electrolysis conditions.[22] Steam reforming catalytic tests, considered by the authors to be propaedeutical to SOC applications, indicate that the concentration of mobile oxygen vacancies on ceria surface may not

---

[a] *Department of Earth Science and Engineering, Imperial College, London SW7 2BP, United Kingdom*

[b] *Department of Physics, Imperial College, London SW7 2BP, United Kingdom*

[c] *Department of Mechanical Engineering, Imperial College, London SW7 2BP, United Kingdom*

[±] *v.duboviks11@imperial.ac.uk*

always be sufficient to inhibit carbon deposition.[23] Thus, the focus of this study is on the effect of the negative bias applied to Ni/CGO electrodes exposed to a CO-CO_2 gas mixture at low temperature (500 °C). Such conditions are likely to promote carbon deposition as the result of the following reactions:

$$CO_{2(ad)} + 4e^{-} \leftrightarrows C_{(ad)} + 2O^{2-} \quad (1)$$

$$CO_{(ad)} + 2e^{-} \leftrightarrows C_{(ad)} + O^{2-} \quad (2)$$

$$2CO_{(ad)} \leftrightarrows C_{(ad)} + CO_2 \quad (3)$$

In SOFCs carbon deposition is also well know and several methods have been suggested to mitigate it. The balance of the reactions (1) and (2) may be shifted towards oxidation of the adsorbed carbon by providing a large influx of O^{2-} to the fuel electrode. It has been shown that virtually all electrochemically accessible graphite formed after CH_4 exposure may be oxidized in this way.[24] The forward Boudouard reaction (3) is suppressed if CO_2 is present in sufficient quantities. Additionally, control of the gas composition within the fuel electrode using barrier layers can improve SOFC stability. Inserting a chemically inert barrier layer between the gas phase and the electrode was shown to inhibit carbon formation by limiting the flux of CH_4 into the fuel electrode and the flux of H_2O and CO_2 out.[25] Simulations suggests that barrier layers may also assist in decreasing thermal-mechanical stresses by moderating endothermic reactions on the fuel electrode.[26] However, this cannot be directly translated to the SOEC case, because the flow of the chemical species is reversed.

Raman spectroscopy is ideally suited to the identification of molecular structures present on electrode surfaces.[27,28] It has previously been applied to the study of carbon deposition on Ni/YSZ[29–31] as well as Ni/CGO anodes.[32] Eigenbrodt et al., reported spatially resolved spectroscopic measurements suggestive of an extension in the electrochemically active region to 10μm around the triple phase boundary (TPB) in the Ni/YSZ system.[33] Yoshinaga et al., employed Raman mapping to demonstrate that carbon deposition may be suppressed for the Ni/CGO system particularly on large nickel particles.[20] *In situ* Raman studies of a patterned electrode stimulated the development of a novel carbon-tolerant material for SOFC anodes.[34,35] However, it remains unclear how representative surface measurements are of the entire electrode. The present work demonstrates results derived by applying this technique to electrolysis conditions and performing cross sectional *ex situ* Raman analysis on the electrodes.

For the *in situ* experiments, a revised version of the experimental rig described elsewhere was employed.[36] It was modified such that the inner core was made out of alumina and a sapphire window was used for optical access. The updated design of the rig is shown in Figure 1. Current collection was performed by applying a small amount of gold paste between the gold mesh and the electrode on both sides. *In situ* measurements were performed using a Horiba Jobin Yvon LabRAM 800 HR Raman spectrometer. *Ex situ* Raman measurements were taken with a Renishaw RM-2000 CCD spectrometer equipped with ×20 and ×50 short working distance objectives. All spectra were collected using a 514nm Argon ion laser which was focused onto the sample surface in a spot size of approximately 3μm diameter. Incident laser power was maintained at approximately 5 mW throughout all measurements to ensure laser interaction with the surfaces was minimised. Raman spectral peaks were fitted and integrated using the Renishaw Wire 2 software with further analysis performed in OriginLab.

Electrolyte-supported button cells with porous Ni/CGO and Ni/YSZ electrodes were employed. A Ni/CGO ink with 60% NiO – 40% CGO by weight was used for the preparation of the electrodes. The ink was screen printed onto a 20 mm in diameter and 270 μm thick YSZ substrate and sintered for 2 hr at 1300 °C resulting in a ~7 μm thick 0.5 cm^2 porous electrode. A CGO10 interlayer was screen printed on the other side of the electrolyte to prevent $SrZrO_3$ and $La_2Zr_2O_7$ phase formation.[37,38] The CGO10 interlayer was sintered for 2hr at 1300 °C after which the CGO10/$(La_{0.6}Sr_{0.4})(Co_{0.2}Fe_{0.8})O_{3-\delta}$ air electrode was screen printed on top of the interlayer and sintered at 900 °C for 2 hours.[38]

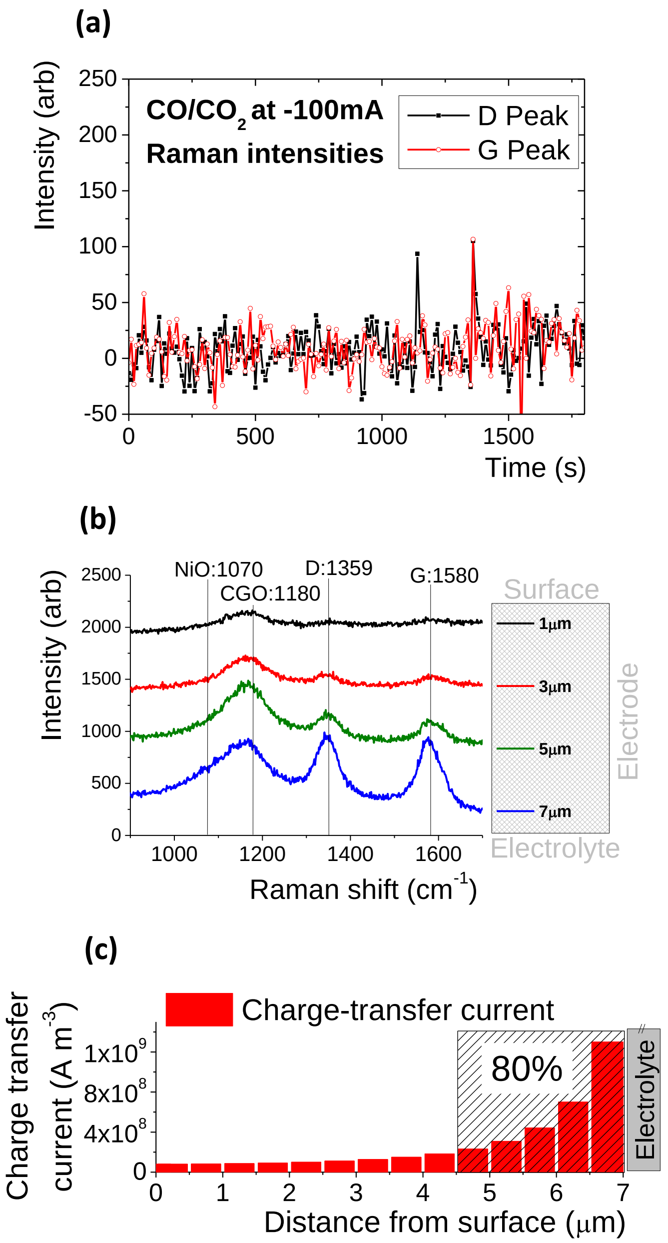

Fig. 2 (a) Integrated D and G peak areas obtained from spectra collected *in situ* from the surface of Ni/CGO electrode as a function of time during the electrode exposure to CO-CO_2 with -100 mA bias. (b) Raman spectra collected *ex situ* from the cross section of Ni/CGO electrode along a single line at different distances from the surface (1 μm being adjacent to the surface) after 30 min exposure to CO-CO_2 with -100 mA bias. (c) Numerical simulation of charge-transfer current distribution in the electrode in these conditions.

The cells were heated up to 500 °C under N_2 flow on the fuel electrode after which 50 ml/min of H_2 was added to the fuel compartment for at least 1hr to fully reduce the electrode. Each cell was fully characterised using a series of electrochemical measurements in order to ensure that it was functional and comparable. The H_2 was then replaced by 50 ml/min of CO plus 50 ml/min of CO_2. Normally, the gas composition along the flow channel of a commercial SOEC will change as the reactants are converted into products.[39] However, in this case fuel utilization is less than 2% and it can therefore be assumed that the gas composition does not significantly change across the electrode in the flow direction. Therefore, the gas mixture chosen for the tests can be considered to represent one point in the flowfield of a commercial SOEC.

The cell was allowed to stabilize at open circuit potential (OCP) for one minute. N_2 was then switched off and the cell was polarized so that a current of 100 mA was passed through it (electrolysis mode) for 30 min. After that, the supply of current and CO/CO_2 fuel to the cell were turned off and the rig was cooled to room temperature under N_2 flow on the fuel electrode. Pellets were taken out of the rig and prepared for further cross sectional analysis with Raman spectroscopy. No electrochemical tests were run on the cells after the CO-CO_2 experiments to avoid any additional changes before the *ex situ* analysis.

It was previously shown that positive bias (fuel cell mode) assists in removing carbon from contaminated electrodes.[24,40] In electrolysis conditions O^{2-} is removed from the fuel electrode, making carbon deposition more favourable.[41] However, no carbon was observed *in situ* on the surface of the electrode as shown in Figure 2a. Potential monitoring (not shown) also did not reveal any significant changes to electrode performance. The penetration depth of the laser used in the Raman experiments is typically limited to the uppermost layer of the electrode. According to the Beer-Lambert law, pure solid nickel having an absorption coefficient of $7.44 \cdot 10^7$ m at 514 nm[42], would have the penetration depth δ of around 13.4 nm. However, the porous nature of the Ni/CGO electrodes is likely to extend this value to a few hundred nanometres, suggesting that only changes occurring within a thin upper layer of the electrolyte will be detected. Therefore, despite the fact that surface *in situ* Raman analysis indicates the absence of carbon, an *ex situ* cross sectional analysis is essential in order to confirm or refute this result.

In order to perform the *ex situ* Raman analysis, cells that underwent testing were carefully snapped and 1D Raman maps were collected from the cross section of the Ni/CGO electrodes. Snapping rather than cutting of the samples is preferred in order to prevent contamination of the sample. A spectral region with carbon D (1359 cm^{-1}) and carbon G (1580 cm^{-1}) peaks as well as the NiO peak (around 1070 cm^{-1})[29,43,44] overlapping with the secondary CGO peak (1180 cm^{-1})[45] is shown in Figure 2b. Spectra were taken along a single line at different distances from the surface, 1 µm being adjacent to the surface and 7 µm – next to electrolyte. The curves have been offset for clarity. The shown data is from a single line scan but several line maps have been analysed to ensure that the shown data is representative of the whole sample. An increase in the Raman signal intensity between 1100cm^{-1} and 1200cm^{-1} in Figure 2b is likely to represent the change in oxidation state of the sample. Both the decreased density of oxygen vacancies in the CGO phase and the oxidation of the Ni phase would lead to an increase in Raman intensity between 1100cm^{-1} and 1200cm^{-1}. Therefore, the spectra in Figure 2b may suggest transport of oxygen from the surface towards the electrode-electrolyte interface.

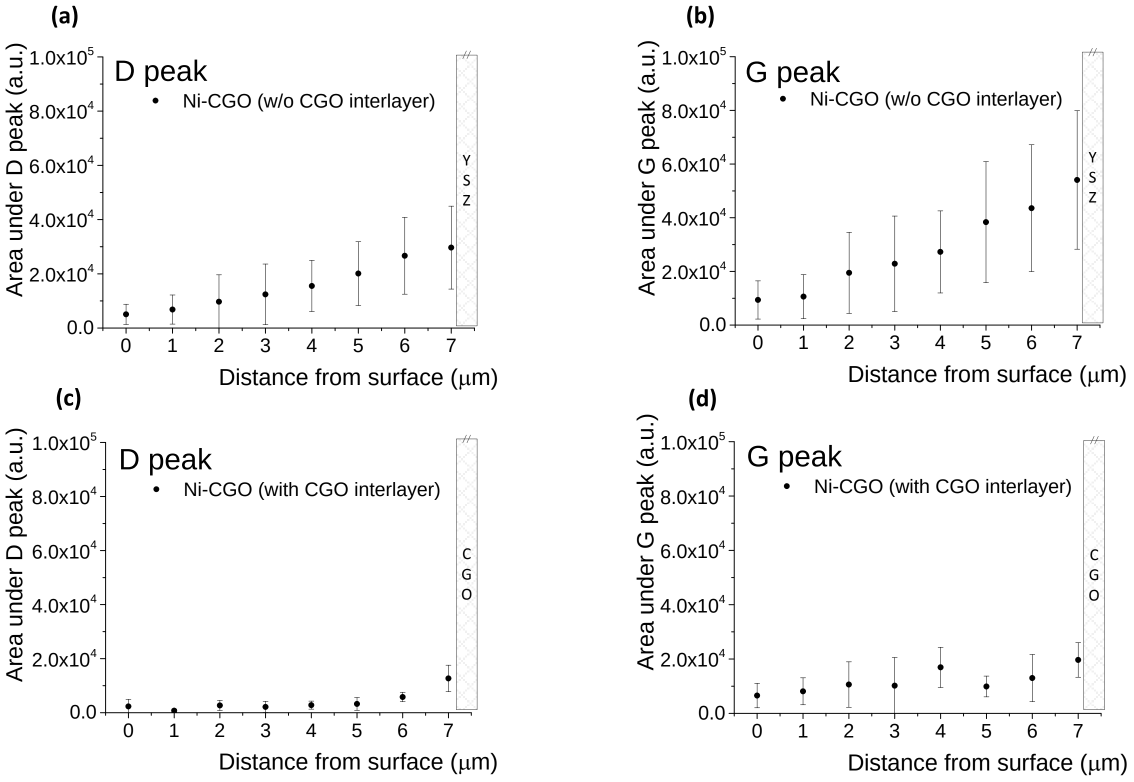

Fig. 3 Integrated carbon peak areas obtained from spectra collected *ex situ* from the cross section of Ni/CGO electrodes as a function of distance from the electrode-gas interface to the electrode-electrolyte interface after 30 min of exposure to CO-CO_2 with -100 mA bias (electrolysis mode). (a) Integrated D peak (1359 cm^{-1}) and (b) G peak (1580 cm^{-1}) for the electrode without CGO interlayer. (c) Integrated D peak (1359 cm^{-1}) and (d) G peak (1580 cm^{-1}) for the electrode with CGO interlayer.

The data in Figure 2b also suggests a trend of increased carbon formation close to the electrode-electrolyte interface. A D/G ratio of ~0.5 indicated the formation of amorphous carbon. An important repercussion of these results is that *in situ* Raman observations in electrolysis mode may therefore be misleading. As discussed above, Raman spectroscopy is well suited for surface characterisation, but does not provide the information about the changes in the bulk of the electrolyte. In order to understand the nature of the preferential carbon formation close to the electrode-electrolyte, a numerical simulation of the charge-transfer current density has been performed.

Distribution of the charge-transfer current density in the electrodes was estimated using the model described in detail elsewhere.[46] The conservation of electrons and ions in solid phases was described in terms of the electric potential in each phase. Gaseous diffusion of CO and CO_2 in the porous electrode was considered using the dusty-gas model.[47] As the actual thickness of the electrodes was approximately 7 µm, this thickness was assumed for the model. As shown in Figure 2c, most of the electrochemical reactions occur within 3 µm of the electrolyte-electrode interface. This is mostly because gas diffusion and electron conduction through the cermet electrode is much more facile than oxide ion transport. This means that there is also a local increase in CO concentration next to the electrode-electrolyte interface, which will increase the thermodynamic driving force for carbon formation. It is therefore reasonable to conclude that the applied negative bias has resulted in the increased carbon deposition in the vicinity of the electrolyte-electrode interface through local variation in gas composition. Equally, relatively high concentration of CO_2 next to the surface of the electrode may explain the absence of carbon in this region, as CO_2 is an effective reagent for removing accumulated carbon through dry reforming.[48]

CO is known to cause mechanical degradation, e.g. dusting of Ni.[49] Carbon diffusion into the bulk of the metal can occur in case of weak metal-carbon bonding.[50,51] Coadsorption experiments have shown that if H_2 is present in the gas mixture, when adsorbed on the metal, it diminishes the chemisorption bond energy of CO.[52] Subsequently, the probability of electron transfer from the CO orbital into the metal d orbital is decreased and it is reflected in the bonding development between metal and carbon, enabling carbon diffusion.[50] Thus, in presence of H_2, a profuse Ni graphitization leading to unlimited growth of highly amorphous carbon may be expected. Whereas at high CO/H_2 ratios, or equally in pure CO, the carbon-transfer rate to the metal surface is relatively slow and most of the carbon is catalysed by the metal surface to form a surface deposit.[49]

In the absence of hydrogen, carbon deposition can proceed either through carbon monoxide disproportionation or through the reaction with oxygen vacancies. It has been found that the most stable form of carbon on Ni(111) is the highly ordered graphite overlayer.[53] Nolan et al. experimentally observed the formation of carbon in the form of lamellar graphite layers extending parallel to the surface of the Ni particle and eventually deactivating it.[54] Therefore, carbon in these experiments may be expected to form highly structured encapsulating layers on top of the Ni particles. By examining the relative intensities of G and D peaks in Figure 2b, it can be concluded that this is not strictly the case. The D peak is a breathing mode of A_{1g} symmetry and is forbidden in perfect graphite.[55] We therefore argue that if encapsulating structures do form then they must have a significant defect density.

Electrode delamination has been reported during co-electrolysis at high current densities both for Ni/YSZ and Ni/CGO electrodes.[13,41] In the former case it was ascribed to the growth of carbon fibres leading to a volume expansion. Here, the feasibility of CGO interlayers to improve the robustness of Ni/CGO electrodes to carbon formation is explored. CGO interlayers are commonly employed for LSCF-based air electrodes to avoid the formation of non-conductive phases between the electrode and the electrolyte.[37] More importantly it has also been shown to improve the adhesion between the electrode and electrolyte.[56] Additionally, CGO microparticles were reported to increase the durability and performance of electrolysis cells.[22] The investigation of the effect of CGO interlayer when applied to the fuel electrode in the current work is motivated by these reports.

Figure 3 shows the results of line mapping of the integrated Raman spectral peaks at 1359 cm^{-1} (D) and 1580 cm^{-1} (G) collected with 1 µm pixel resolution. To ensure the data is representative, several different locations were examined on at least two different electrodes exposed to identical conditions. Figure 3 shows the averaged values obtained from these measurements with error bars representing the standard deviation. There are at least two likely sources of relatively large deviation from the average value. First is the roughness of the porous electrode's cross section. The intensity of Raman peaks depends on the area from which the data is collected – when the surface is rough there is therefore a difference in the size of the analysed area. Secondly, although every effort was made to ensure homogeneous current distribution in the electrode, current collection with a mesh, as performed in these experiments, induces a certain current inhomogeneity, which may cause differences in amount of deposited carbon.

Ceria is well known for its high electrochemical activity.[57] It is generally accepted that the prevalent mechanism of CO oxidation on ceria involves a redox Mars–van Krevelen-type reaction, where CO reacts with the weakly bound, topmost oxygen atom and forms CO_2 that desorbs leaving an oxygen vacancy behind.[58] For Ni/CGO without an interlayer the results shown in Figure 3 suggest that in electrolysis mode a reverse reaction may take place on CGO close to the TPB region, i.e. electrolysis gives rise to the oxygen vacancies, which react with CO to produce carbon deposits, as shown in equation 2. The results presented in Figure 3 also suggest that the presence of the ~10 µm CGO interlayer between Ni/CGO electrode and YSZ electrolyte helps to suppress carbon formation under electrolysis, for at least the duration of the experiment. It is assumed that the CGO interlayer provide an additional source of oxygen atoms, helping to reduce carbon deposition.

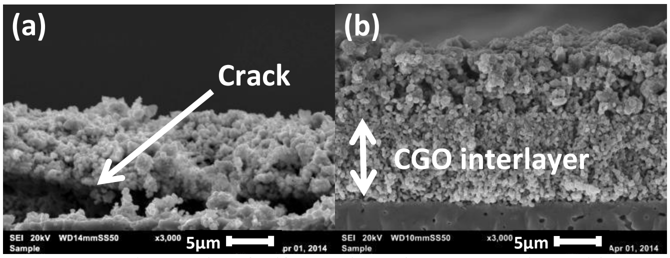

Fig. 4 SEM micrographs of Ni/CGO electrodes' cross sections without (a) and with (b) CGO interlayer.

Scanning electron microscope (SEM) micrographs in Figure 4 show that electrodes without the interlayer tend to develop cracks between the electrode and the electrolyte, whereas the electrodes with the interlayer retain good adhesion. Impregnating fuel electrodes with ceria has also been shown to prevent electrode delamination caused by carbon.[59] The CGO interlayer presented here demonstrates that such an interlayer improves the adhesion between the electrolyte and the electrode, helping to prevent delamination in electrolysis mode. Fuel electrodes on two out of three samples without the CGO interlayer were partially delaminated, while all of the samples with the CGO interlayer seemed to remain structurally robust.

Conclusions

Charge-transfer reactions that occur at the TPB in CO_2 electrolysis mode were shown to promote carbon deposition through local changes in gas composition. *Ex situ* Raman mapping was used in conjunction with numerical modelling to show that most of the carbon forms close to electrode-electrolyte interface during CO-CO_2 electrolysis. This represents a potential limitation of the Raman *in situ* technique when applied to SOECs, which must be carefully considered in relation to the experimental conditions. As a surface sensitive technique, it is not fully representative of interactions occurring within the bulk of the electrode. As a result, a better understanding of interactions within SOCs is obtained through a combination of *in-situ* and *ex-situ* Raman and other analysis techniques. The results of *ex situ* Raman and SEM analysis suggest that the CGO interlayer acts to reduce carbon deposition in Ni/CGO electrodes as well as improving the mechanical stability in CO-CO_2 electrolysis conditions.

Acknowledgements

The authors would like to thank the Engineering and Physical Sciences Research Council (U.K.) EPSRC(GB)) for funding, in particular the Supergen fuel cell programme and a Career Acceleration Fellowship for Gregory Offer and funding under EP/J003085/1 (RCM), and Stephen Cussell in the engineering workshop of the Department of Physics.

Notes and references

1. A. O. Isenberg, *Solid State Ionics*, 1981, **3/4**, 431–437.
2. Q. Fu, C. Mabilat, M. Zahid, A. Brisse, and L. Gautier, *Energy Environ. Sci.*, 2010, **3**, 1382.
3. S. H. Jensen, P. H. Larsen, and M. Mogensen, *Int. J. Hydrogen Energy*, 2007, **32**, 3253–3257.
4. C. M. Stoots, J. E. O'Brien, J. S. Herring, and J. J. Hartvigsen, *J. Fuel Cell Sci. Technol.*, 2009, **6**, 011014.
5. Z. Zhan, W. Kobsiriphat, J. R. Wilson, M. Pillai, I. Kim, and S. A. Barnett, *Energy & Fuels*, 2009, **23**, 3089–3096.
6. J. E. O'Brien, M. G. McKellar, E. A. Harvego, and C. M. Stoots, *Int. J. Hydrogen Energy*, 2010, **35**, 4808–4819.
7. S. D. Ebbesen, C. Graves, and M. Mogensen, *Int. J. Green Energy*, 2009, **6**, 646–660.
8. G. J. Offer, J. Mermelstein, E. Brightman, and N. P. Brandon, *J. Am. Ceram. Soc.*, 2009, **92**, 763–780.
9. V. Alzate-Restrepo and J. M. Hill, *J. Power Sources*, 2010, **195**, 1344–1351.
10. C. M. Finnerty, N. J. Coe, R. H. Cunningham, and R. M. Ormerod, *Catal. Today*, 1998, **46**, 137–145.
11. H. He and J. M. Hill, *Appl. Catal. A Gen.*, 2007, **317**, 284–292.
12. J. Mermelstein, M. Millan, and N. P. Brandon, *Chem. Eng. Sci.*, 2009, **64**, 492–500.
13. Y. Tao, S. D. Ebbesen, and M. B. Mogensen, *J. Electrochem. Soc.*, 2014, **161**, F337–F343.
14. Y. Liu and C. Jiao, *Solid State Ionics*, 2005, **176**, 435–442.
15. K. Girona, J. Laurencin, J. Fouletier, and F. Lefebvre-Joud, *J. Power Sources*, 2012, **210**, 381–391.
16. A. Utz, A. Leonide, A. Weber, and E. Ivers-Tiffée, *J. Power Sources*, 2011, **196**, 7217–7224.
17. B. Yildiz and M. Kazimi, *Int. J. Hydrogen Energy*, 2006, **31**, 77–92.
18. S. P. Jiang and S. H. Chan, *J. Mater. Sci.*, 2004, **39**, 4405–4439.
19. P. Kim-Lohsoontorn and J. Bae, *J. Power Sources*, 2011, **196**, 7161–7168.
20. M. Yoshinaga, H. Kishimoto, K. Yamaji, Y.-P. Xiong, M. E. Brito, T. Horita, and H. Yokokawa, *Solid State Ionics*, 2011, **192**, 571–575.
21. H. Kishimoto, T. Shimonosono, K. Yamaji, M. E. Brito, T. Horita, and H. Yokokawa, *Electrochemistry*, 2013, **81**, 255–258.
22. P. Kim-Lohsoontorn, Y.-M. Kim, N. Laosiripojana, and J. Bae, *Int. J. Hydrogen Energy*, 2011, **36**, 9420–9427.
23. V. Modafferi, G. Panzera, V. Baglio, F. Frusteri, and P. L. Antonucci, *Appl. Catal. A Gen.*, 2008, **334**, 1–9.
24. J. D. Kirtley, D. M. Halat, M. D. McIntyre, B. C. Eigenbrodt, and R. A. Walker, *Anal. Chem.*, 2012, **84**, 9745–53.
25. H. Zhu, A. M. Colclasure, R. J. Kee, Y. Lin, and S. A. Barnett, *J. Power Sources*, 2006, **161**, 413–419.
26. M. Pillai, Y. Lin, H. Zhu, R. J. Kee, and S. A. Barnett, *J. Power Sources*, 2010, **195**, 271–279.
27. J. R. Ferraro, K. Nakamoto, and C. W. Brown, *Introductory Raman Spectroscoy*, Elsevier Science, USA, 2nd edn., 2008.
28. Z. Cheng, J.-H. Wang, Y. Choi, L. Yang, M. C. Lin, and M. Liu, *Energy Environ. Sci.*, 2011, 4380–4409.
29. M. B. Pomfret, J. C. Owrutsky, and R. A. Walker, *J. Phys. Chem. B*, 2006, **110**, 17305–8.
30. M. B. Pomfret, J. Marda, G. S. Jackson, B. W. Eichhorn, A. M. Dean, and R. A. Walker, *J. Phys. Chem. C*, 2008, 5232–5240.
31. B. C. Eigenbrodt, M. B. Pomfret, D. A. Steinhurst, J. C. Owrutsky, and R. A. Walker, *J. Phys. Chem. C*, 2011, **115**, 2895–2903.
32. R. C. Maher, V. Duboviks, G. J. Offer, M. Kishimoto, N. P. Brandon, and L. F. Cohen, *Fuel Cells*, 2013, **13**, 455–469.
33. B. C. Eigenbrodt and R. A. Walker, *Anal. Methods*, 2011, **3**, 1478.
34. K. S. Blinn, H. Abernathy, X. Li, M. Liu, L. A. Bottomley, and M. Liu, *Energy Environ. Sci.*, 2012, 7913–7917.
35. L. Yang, Y. Choi, W. Qin, H. Chen, K. Blinn, M. Liu, P. Liu, J. Bai, T. a Tyson, and M. Liu, *Nat. Commun.*, 2011, **2**, 357.
36. E. Brightman, R. Maher, G. J. Offer, V. Duboviks, C. Heck, L. F. Cohen, and N. P. Brandon, *Rev. Sci. Instrum.*, 2012, **83**, 053707.
37. A. Mai, V. Haanappel, F. Tietz, and D. Stover, *Solid State Ionics*, 2006, **177**, 2103–2107.
38. E. P. Murray, M. J. Sever, and S. A. Barnett, *Solid State Ionics*, 2002, **148**, 27–34.
39. M. Ni, *Int. J. Hydrogen Energy*, 2012, **37**, 6389–6399.
40. R. C. Maher, V. Duboviks, G. Offer, L. F. Cohen, and N. P. Brandon, *ECS Trans.*, 2013, **57**, 1619–1626.
41. V. Duboviks, R. C. Maher, G. Offer, L. F. Cohen, and N. P. Brandon, *ECS Trans.*, 2013, **57**, 3111–3117.
42. E. Palik, *Handbook of Optical Constants of Solids*, Academic Press, 1998.
43. C. Xu, G. Xu, and G. Wang, *J. Mater. Sci.*, 2002, **38**, 779–782.
44. J. H. Kim and I. S. Hwang, *Nucl. Eng. Des.*, 2005, **235**, 1029–1040.

45. W. H. Weber, K. C. Hass, and J. R. McBride, *Phys. Rev. B*, 1993, **48**, 178–185.
46. M. Kishimoto, H. Iwai, M. Saito, and H. Yoshida, *J. Power Sources*, 2011, **196**, 4555–4563.
47. E. A. Mason, A. P. Malinauskas, and R. B. Evans, *J. Chem. Phys.*, 1967, **46**, 3199.
48. J. Kirtley, A. Singh, D. Halat, T. Oswell, J. M. Hill, and R. A. Walker, *J. Phys. Chem. C*, 2013, **2**.
49. C. M. Chun, J. D. Mumford, and T. A. Ramanarayanan, *J. Electrochem. Soc.*, 2000, **147**, 3680.
50. D. J. Young, J. Zhang, C. Geers, and M. Schütze, *Mater. Corros.*, 2011, **62**, 7–28.
51. Y. Kim, J. H. Kim, J. Bae, C. W. Yoon, and S. W. Nam, *J. Phys. Chem. C*, 2012, **116**, 13281–13288.
52. M. T. Tavares, I. Alstrup, and C. A. Bernardo, *J. Catal.*, 1996, **410**, 402–410.
53. H. Bengaard, J. Noerskov, J. Sehested, B. S. Clausen, L. P. Nielsen, A. . Molenbroeck, and J. R. Rostrup-Nielsen, *J. Catal.*, 2002, **209**, 365–384.
54. P. E. Nolan, D. C. Lynch, and A. H. Cutler, *Carbon N. Y.*, 1994, **32**, 477–483.
55. A. Ferrari and J. Robertson, *Phys. Rev. B*, 2000, **61**, 14095–14107.
56. Y.-M. Kim, P. Kim-Lohsoontorn, and J. Bae, *J. Power Sources*, 2010, **195**, 6420–6427.
57. W. C. Chueh, Y. Hao, W. Jung, and H. M. Sossina, *Nat. Mater.*, 2012, **11**, 155–161.
58. E. Aneggi, J. Llorca, M. Boaro, and A. Trovarelli, *J. Catal.*, 2005, **234**, 88–95.
59. D. J. L. Brett, A. Atkinson, D. Cumming, E. Ramírez-Cabrera, R. Rudkin, and N. P. Brandon, *Chem. Eng. Sci.*, 2005, **60**, 5649–5662.